Supporting information

Transition metal doping enhances pseudocapacitive energy storage in monoclinic molybdenum dioxide

Ze-Dong Zhang [a,b], Guo-Xian Zhao [a,b], Zu-Tao Pan [a,b], Yao Xu [a,b], Ling-Bin Kong [a,b,*]

[a] State Key Laboratory of Advanced Processing and Recycling of Non-ferrous Metals, Lanzhou University of Technology, Lanzhou 730050, P. R. China

[b] School of Materials Science and Engineering, Lanzhou University of Technology, Lanzhou 730050, P. R. China

* Corresponding author. E-mail: konglb@lut.edu.cn

Total number of pages: 11 pages

Number of figures: 9 figures

Number of Tables: 1 table

Material Sources

All the reagents used in the experiment were of analytical grade and used without further purification. Anhydrous molybdenum chloride ($MoCl_5$,>99.5%), Copper chloride dihydrate ($CuCl_2 \cdot 2H_2O$,>99.0%) were purchased from Shanghai Macklin Biochemical Technology Co. Ltd. Ferrous chloride tetrahydrate ($FeCl_2 \cdot 4H_2O$, >99.7%),

Nickel chloride hexahydrate ($NiCl_2 \cdot 6H2O$,>99.0%), Anhydrous zinc chloride ($ZnCl_2$,>98.0%) were purchased from Tianjin Damao Chemical Reagent Factory. Cobalt chloride hexahydrate ($CoCl_2 \cdot 6H_2O$,>99.0%) were purchased from Chengdu Kelong Chemicals Co.Ltd. Anhydrous ethanol (C_2H_5OH) and concentrated sulfuric acid (H_2SO_4) were purchased from Damao Chemical Reagent Factory (Tianjin, China). Acetylene black and graphite were purchased from Shanxi Kaben Trading Co. Steel mesh (99.99%, 1.7 mm) was purchased from Lizhiyuan Co, Ltd (Shanxi, China).

Materials Synthesis

All samples were synthesized via the hydrothermal method. Using $MoCl_5$ as the molybdenum source, 2 mmol of $MoCl_5$ was dissolved at room temperature in a mixed solvent composed of 45 ml deionized water and 15 ml anhydrous ethanol. After stirring for 10 minutes, 1 mmol of ferrous chloride ($FeCl_2$) was added to the solution. The mixture was then stirred in a 70°C water bath for 30 minutes, transferred to an autoclave, and reacted at 180°C for 12 hours in an oven. The resulting precipitate was collected by centrifugation, washed multiple times with ethanol and deionized water, and vacuum-dried overnight at 60°C. Finally, the product was ground to obtain black Fe^{2+}-modified MoO_2 powder. The synthesis of other M-MoO_2 materials followed a procedure analogous to that described above, employing 1 mmol of various transition metal chlorides and 2 mmol of $MoCl_5$.

Material Characterization

Crystal structures of samples were characterized by X-ray diffractometer (XRD, D8 Advance, Bruker Corporation) with Cu Kα radiation ($\lambda = 1.5406$ Å) in the 2θ range of 5° to 90°. Rietveld refinements were carried out using GSAS-II software. The morphologies of the samples and the elemental distribution were investigated by scanning electron microscopy (FESEM5000, CIQTEK Co., Ltd.,). The Chemical state of elements analyzed by X-ray photoelectron spectroscopy (XPS, ESCALAB 250Xi).

Electrode preparation

For a three-electrode configuration, Ag/AgCl electrode, Pt foil, and stencils (1*2 cm) are used as the reference, counter, and working electrodes, respectively. The working electrode consists of 80wt% of the active material, 15wt% of conductivity agent (acetylene black and conducting graphite), and 5wt% of the binder (PTFE), and a few drops of ethanol. 1 M H_2SO_4 aqueous is used as the electrolyte. And in our study, the mass loading is 4 mg cm^{-2}.

Electrochemical evaluation

Cyclic voltammetry (CV) and galvanostatic charge-discharge (GCD) are performed with a CHI660E electrochemical tester. The test is preceded by activation i.e., a scan rate of 100 mV s^{-1} to test the CV three to four times. Electrochemical impedance spectroscopy (EIS) is conducted on an Autolab Potentiostat Galvanostat.

The gravimetric specific capacitance (C_g, F g^{-1}) of the electrode materials can be calculated from the galvanostatic discharged curves according to the following Equation (1):

$$C_g = \frac{I\Delta t}{Vm} \#(1)$$

Where I is the current (mA), V is the potential (V), t is the discharge time (s), and m is the mass of the active material in the electrode (mg).

Electrochemical measurements

The capacitive effects are characterized by analyzing the cyclic voltammetry data at various scan rates according to:

$$i = aV^b \#(2)$$

Where the measured current i obeys a power law relationship with the scan rate ν. Both a and b are adjustable parameters, with b-values determined from the slope of the plot of log i vs log ν. In the eqation, the b-value is 0.5, the electrode material behaves as a battery property, while the b-value is 1, the electrode material exhibits pseudocapacitance properties. And materials with the b-value in the range of 0.5-1 generally exhibit battery properties and pseudocapacitance properties.

Dunn et al. developed an approach to analyze the storage mechanism from the CV curve, where the current response at a fixed potential as being the combination of two separate mechanisms, surface capacitive effects and diffusion-controlled insertion processes:

$$i\ (V)\ = k_1 v + k_2\, V^{\frac{1}{2}} \#(3)$$

Where i (V) is the current response at a fixed potential, ν is the scan rate, k_1 and k_2 are constant at the fixed potential. For analytical purposes, we rearrange this slightly to

$$\frac{i(v)}{V^{\frac{1}{2}}} = k_1\, V^{\frac{1}{2}} + k_2 \#(4)$$

In eq (2), and correspond to the current contributions from the $k_1 v$ $k_2 v^{1/2}$ surface capacitive effects and the diffusion-controlled intercalation process, respectively. Thus, by determining k_1 and k_2, we are able to quantify, at specific potentials, the fraction of the current due to each of these contributions.

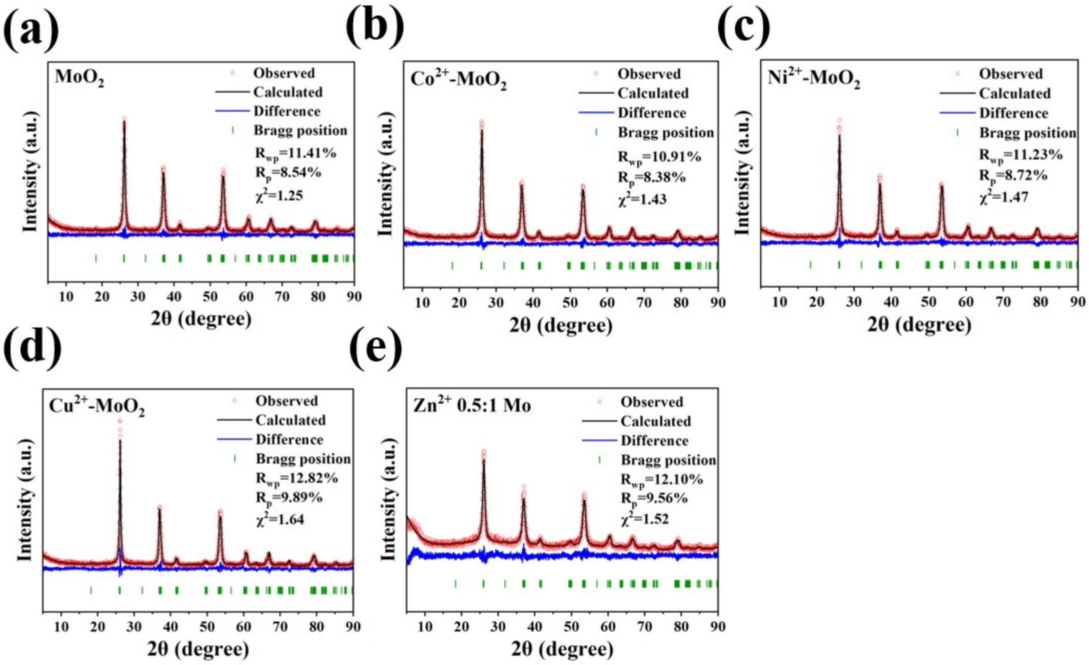

Figure S1. (a) the XRD refinement profiles of Phase-pure MoO_2, (b) Co^{2+}- MoO_2, (c) Ni^{2+}- MoO_2, (d) Cu^{2+}- MoO_2, (e) Zn^{2+}- MoO_2.

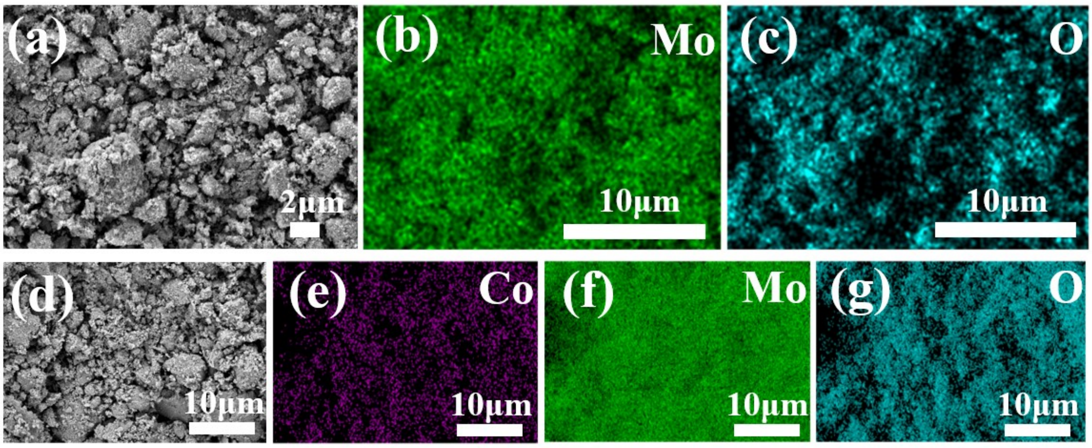

Figure S2. (a–c) the microscopic morphology and element distribution of Phase-pure MoO_2; (d–g) the microscopic morphology and element distribution of Co^{2+}-MoO_2.

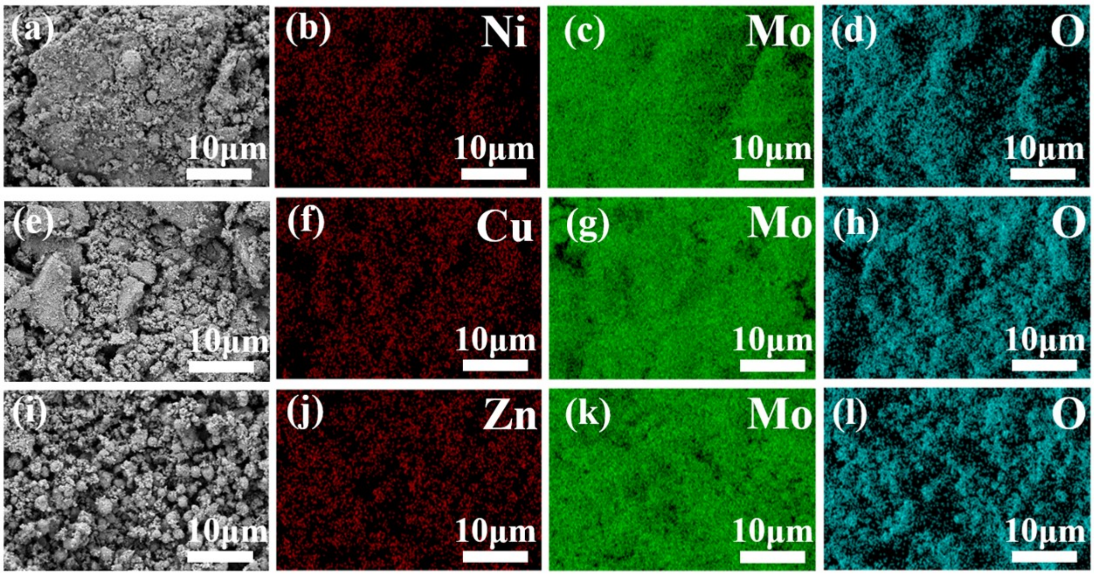

Figure S3. (a–d) the microscopic morphology and element distribution of Ni^{2+}-MoO_2; (e–h) the microscopic morphology and element distribution of Cu^{2+}-MoO_2; (i–l) the microscopic morphology and element distribution of Zn^{2+}-MoO_2.

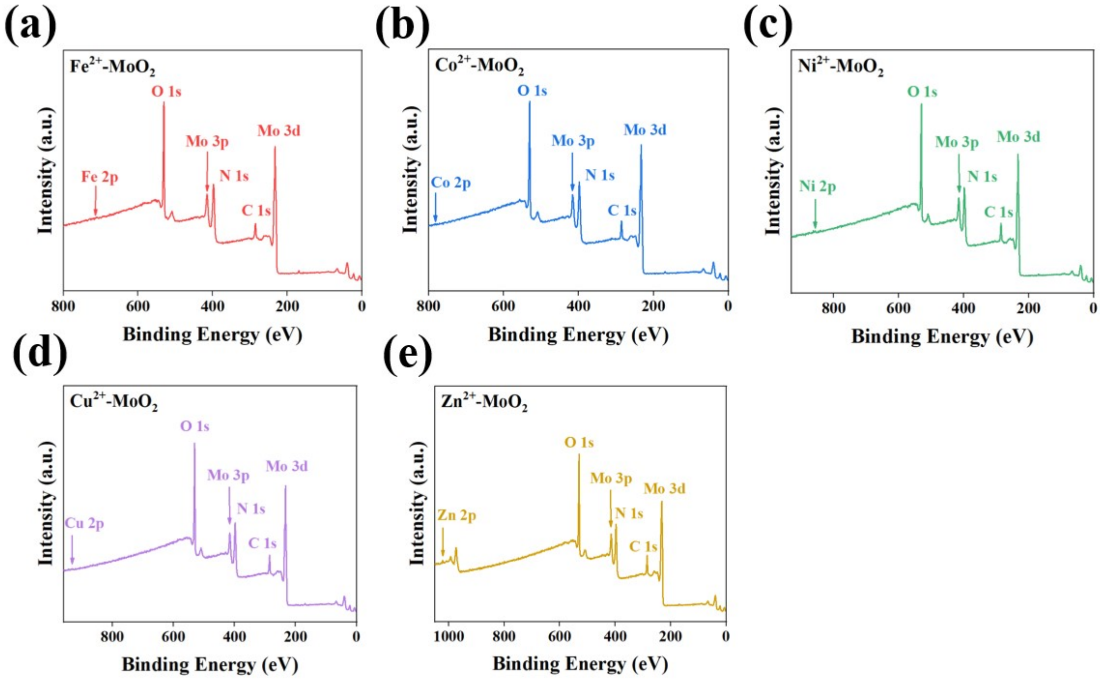

Figure S4. (a) the total XPS spectra of Fe^{2+}-MoO_2; (b) the total XPS spectra of Co^{2+}-MoO_2; (b) the total XPS spectra of Ni^{2+}-MoO_2; (b) the total XPS spectra of Cu^{2+}-MoO_2; (b) the total XPS spectra of Zn^{2+}-MoO_2.

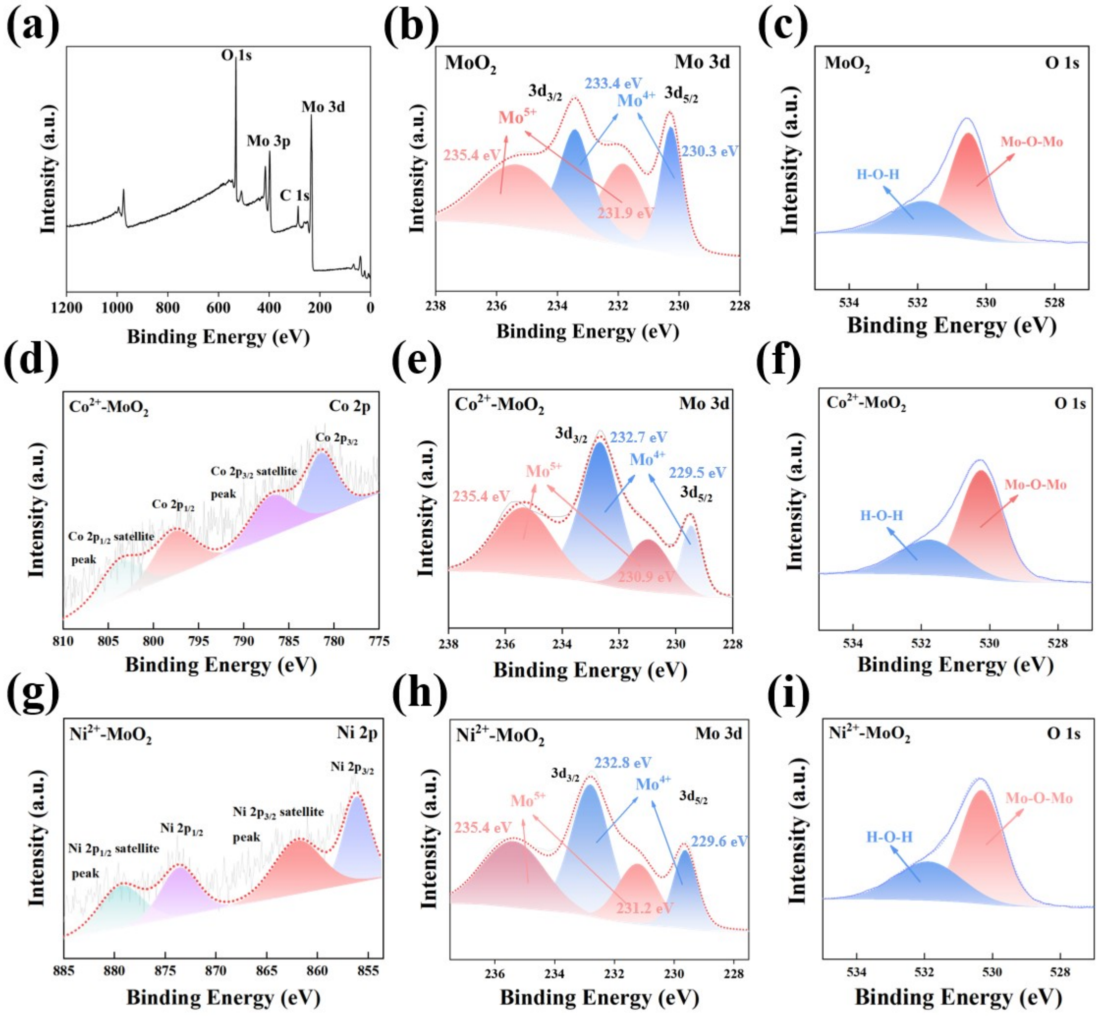

Figure S5. (a) the total XPS spectra of Phase-pure MoO_2; (b, c) Mo high-resolution, and O high-resolution spectra of MoO_2; (d–f) Co high-resolution, and Mo high-resolution, and O high-resolution spectra of Co^{2+}-MoO_2; (g–i) Ni high-resolution, and Mo high-resolution, and O high-resolution spectra of Ni^{2+}-MoO_2.

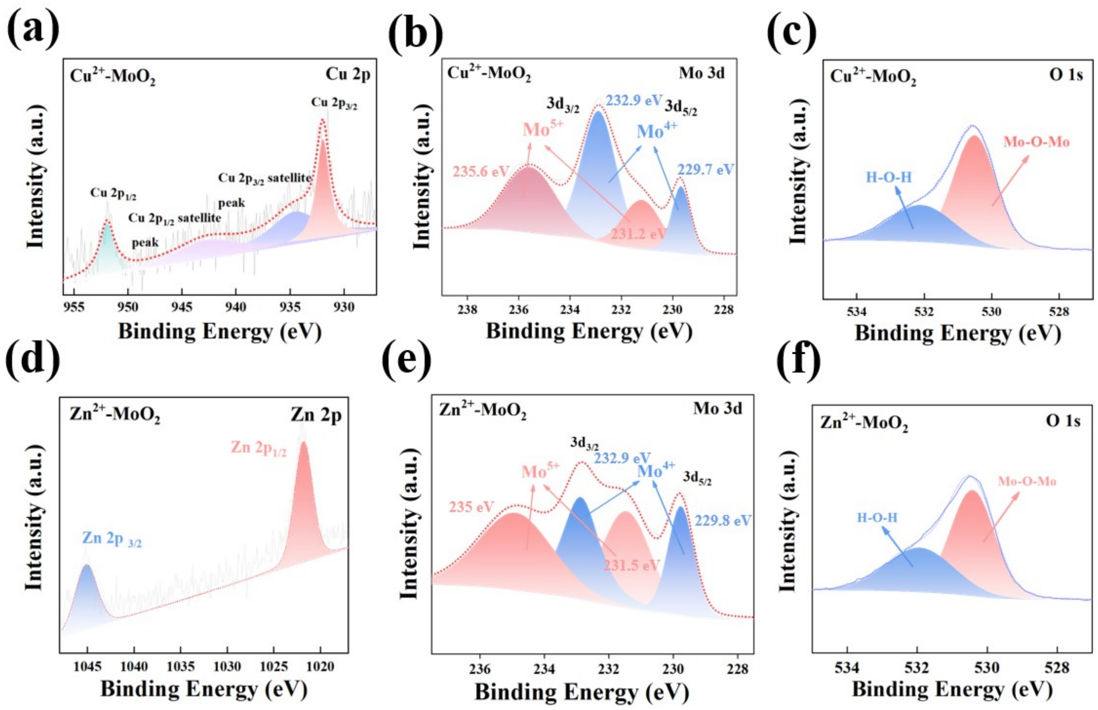

Figure S6. (a-c) Cu high-resolution, and Mo high-resolution, and O high-resolution spectra of Cu^{2+}-MoO_2; (d–f) Zn high-resolution, and Mo high-resolution, and O high-resolution spectra of Zn^{2+}-MoO_2.

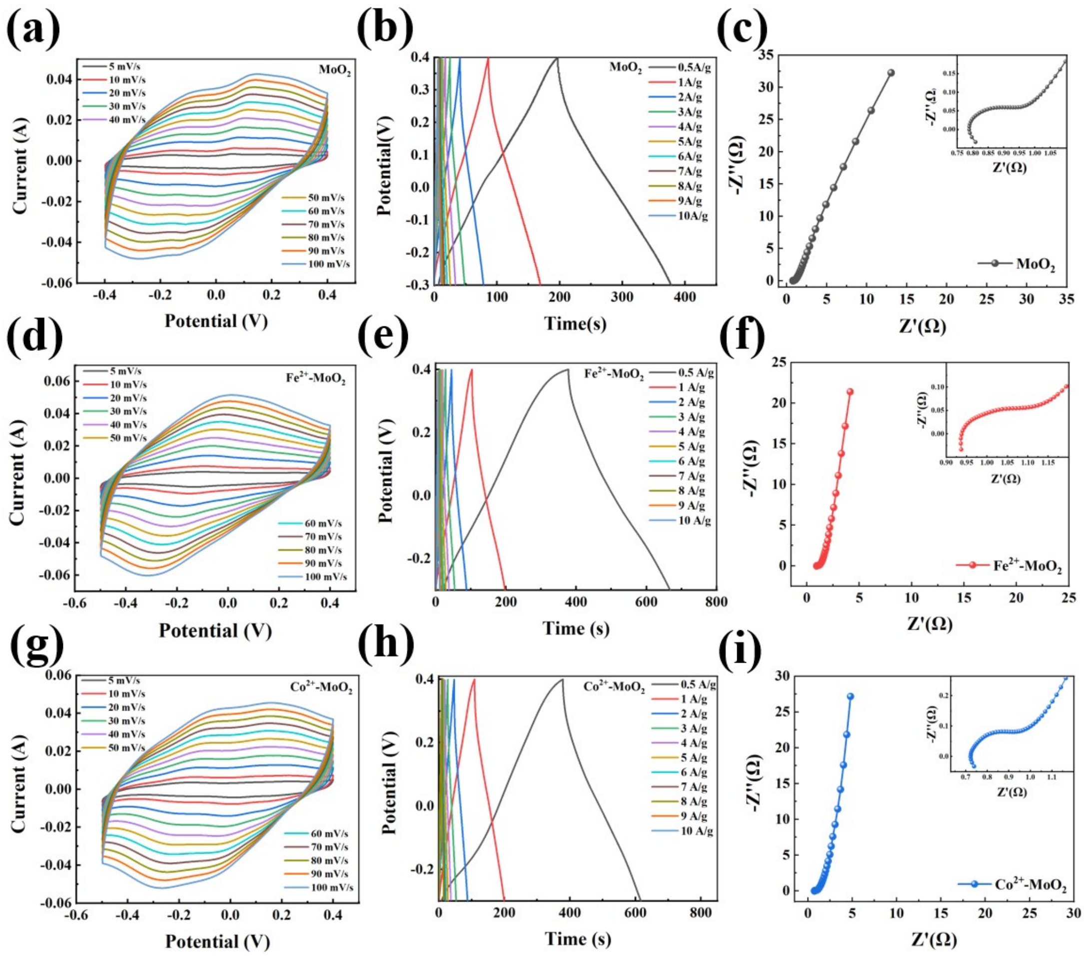

Figure S7. Electrochemical performance tests of Phase-pure MoO$_2$, Fe^{2+}-MoO$_2$, and Co^{2+}-MoO$_2$ electrodes. Including CV curves at different scan rates, GCD curves at different current densities, and EIS plots. (a–c) Phase-pure MoO$_2$; (d–f) Fe^{2+}-MoO$_2$; (g–i) Co^{2+}-MoO$_2$.

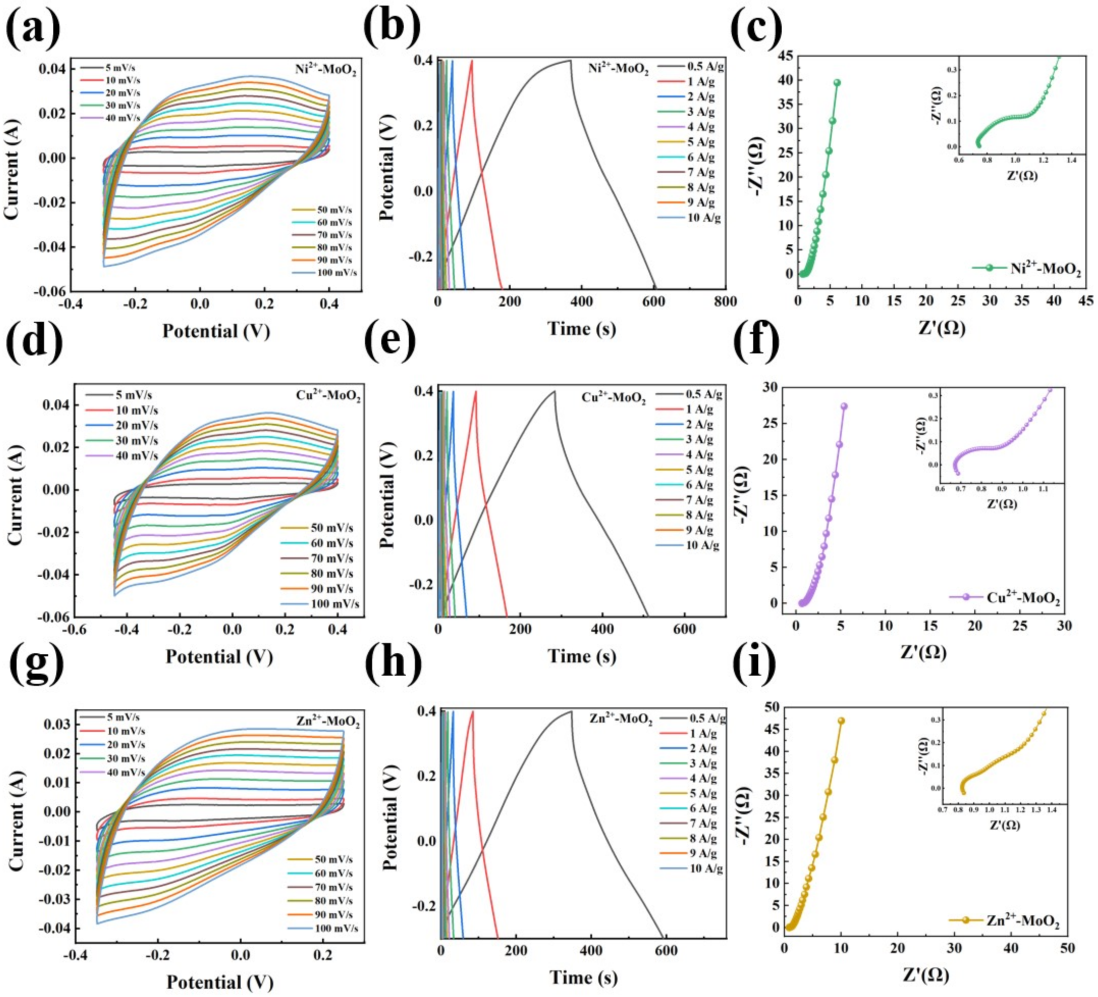

Figure S8. Electrochemical performance tests of Phase-pure Ni^{2+}-MoO$_2$, Cu^{2+}-MoO$_2$, and Zn^{2+}-MoO$_2$ electrodes. Including CV curves at different scan rates, GCD curves at different current densities, and EIS plots. (a–c) Ni^{2+}-MoO$_2$; (d–f) Cu^{2+}-MoO$_2$; (g–i) Zn^{2+}-MoO$_2$.

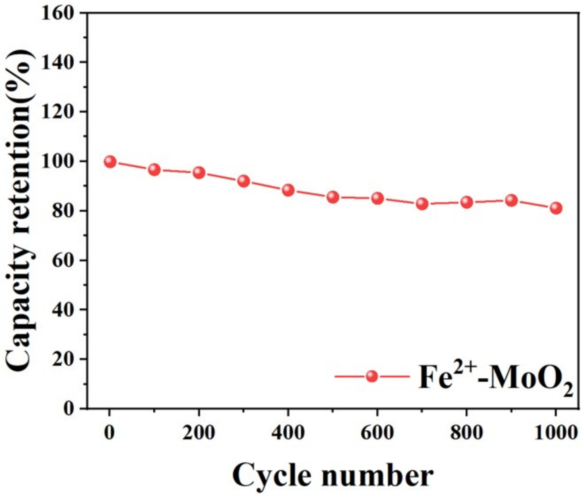

Figure S9. Cyclic stability test of Fe^{2+}-MoO_2.

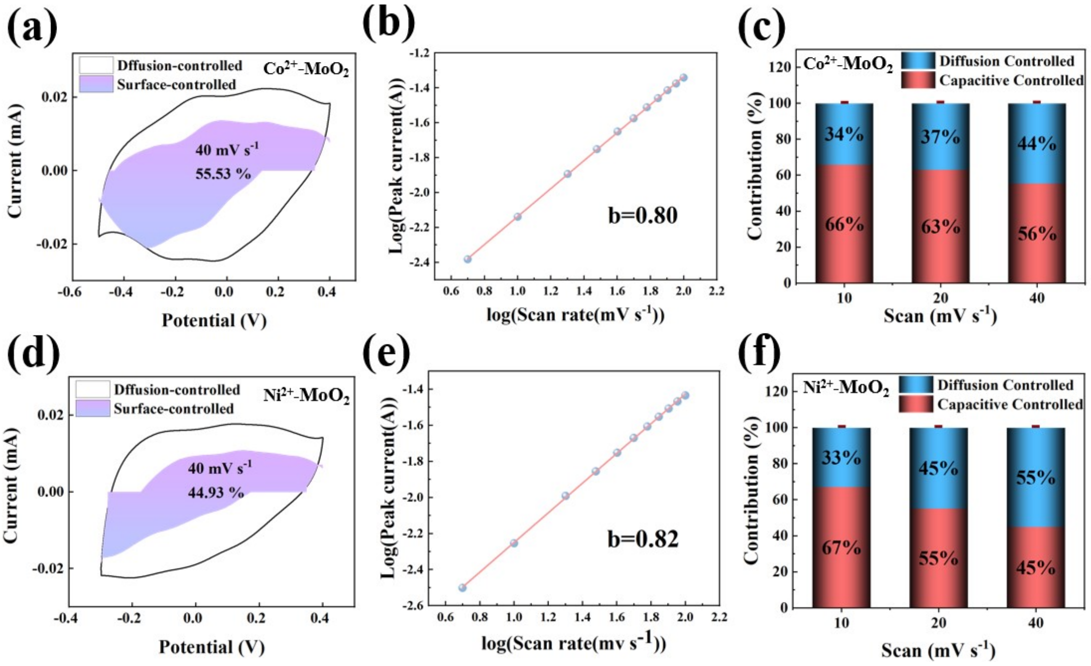

Figure S10. Electrochemical kinetic analysis of Co^{2+}-MoO_2, Ni^{2+}-MoO_2 electrodes. Includes contributions to surface capacitance and diffusion control at 40 mV s^{-1}, b-value analysis, and histograms of capacitance contributions at different sweep speeds. (a–c) Co^{2+}-MoO_2; (d–f) Ni^{2+}-MoO_2.

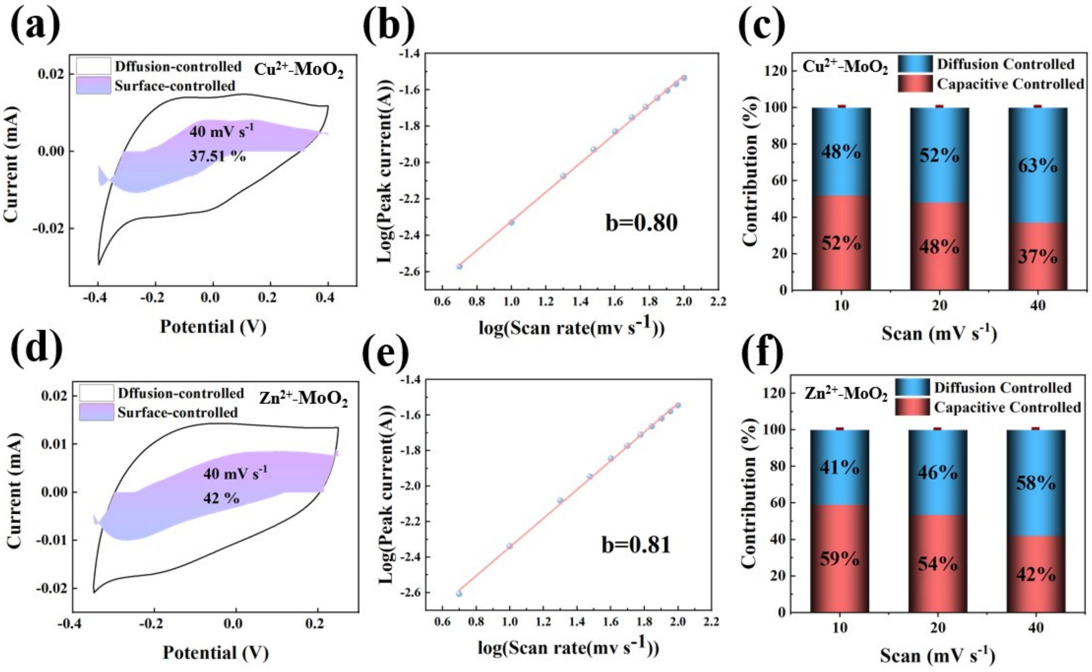

Figure S11. Electrochemical kinetic analysis of Cu^{2+}-MoO_2, Zn^{2+}-MoO_2 electrodes. Includes contributions to surface capacitance and diffusion control at 40 mV s^{-1}, b-value analysis, and histograms of capacitance contributions at different sweep speeds. (a–c) Cu^{2+}-MoO_2; (d–f) Zn^{2+}-MoO_2.

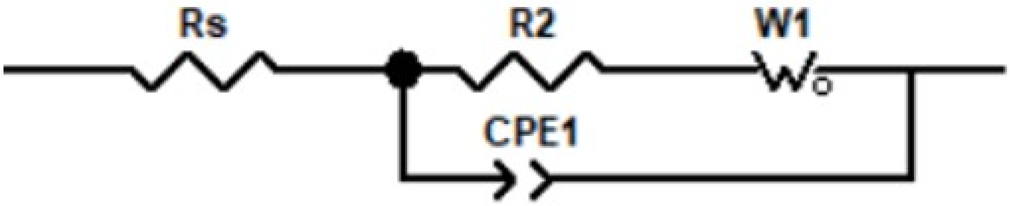

Figure S12. The equivalent circuit model used to fit the Nyquist plots.

Table S1. The Lattice parameters of all samples. obtained from Rietveld refinement of powder XRD data using GSAS-II.

	a (Å)	b (Å)	c (Å)	V (Å^3)	β(°)	R_{wp}	R_p	χ^2
MoO_2	5.642	4.839	5.598	131.428	120.693	11.41%	8.54%	1.25
Fe^{2+}-MoO_2	5.653	4.830	5.56	130.980	120.266	7.87%	6.26%	1.20
Co^{2+}-MoO_2	5.646	4.839	5.562	131.481	120.113	10.91%	8.38%	1.43
Ni^{2+}-MoO_2	5,640	4.8432	5.604	131.64	120.692	11.23%	8.72%	1.47
Cu^{2+}-MoO_2	5.641	4.8327	5.561	131.107	120.131	12.82%	9.89%	1.64
Zn^{2+}-MoO_2	5.639	4.8467	5.61	131.881	120.67	12.10%	9.56%	1.52

Table S2. Electrochemical Performance Comparison of As-Prepared Fe^{2+}-MoO_2 with Previously Reported Molybdenum-Based Oxide Electrode Materials.[1-5]

Material System and Synthesis Method	Specific Gravimetric Capacitance	Energy Density
Fe^{2+}-MoO_2 (This work)	206.4 F g^{-1} at 0.5 A g^{-1}	23.22 Wh kg^{-1}
Preparation of MoO_2 Nanospheres via Ethylene Glycol-Assisted Hydrothermal Method	204.7 F g^{-1} at 0.5 A g^{-1}	Not reported
Ice-flower structured MoO_2 was prepared via in-situ hydrothermal growth.	Not reported	20.19 Wh kg^{-1}
Three-dimensional carbon-based MoO_2 composite material	411.1 F g^{-1} at 0.5 A g^{-1}	14 Wh kg^{-1}
MoS_2/MoO_2@CNT nanocomposite	228.4 F g^{-1} at 0.5 A g^{-1}	11.88 Wh kg^{-1}
MoO_2/MoO_3 core-shell structure	192 F g^{-1} at 0.5 A g^{-1}	Not reported

Table S3. Fitted parameters of the Nyquist plots for MoO_2 and Fe^{2+}-MoO_2.

Electrodes	Rct[Ω]
MoO_2	0.085733
Fe^{2+}-MoO_2	0.11828

References

1 P. Ou, Q. Zhou, J. Li, W. Chen, J. Huang, L. Yang, J. Liao, M. Sheng, Facile ethylene glycol-assisted hydrothermal synthesis of MoO2 nanospheres for high–performance supercapacitors, Materials Research Express 6 (2019) 095044.

2 S. Wang, Z. Qiu, L. Li, H. Zheng, J. Wang, J. Zhang, M. Wang, Z. Tan, Q. Zhuang, Energy Storage Performance of Environmentally Friendly Lotus Petiole–Porous Carbon Composites, The Journal of Physical Chemistry C 127 (2023) 6125-6134.

3 W. Zhu, X. Yan, X. Huang, S. Wu, H. Chen, J. Pan, T. Li, Z. Shahnavaz, Three-dimensional carbon-based endogenous-exogenous MoO2 composites as high-performance negative electrode in asymmetric supercapacitors and efficient electrocatalyst for oxygen evolution reaction, Ceramics International 49 (2023) 5646-5656.

4 S. Fang, D. Bresser, S. Passerini, Transition Metal Oxide Anodes for Electrochemical Energy Storage in Lithium- and Sodium-Ion Batteries, Advanced Energy Materials 10 (2020) 1902485.

5 Y. Tian, H. Du, M. Zhang, Y. Zheng, Q. Guo, H. Zhang, J. Luo, X. Zhang, Microwave synthesis of MoS2/MoO2@CNT nanocomposites with excellent cycling stability for supercapacitor electrodes, Journal of Materials Chemistry C 7 (2019) 9545-9555.